Bending-induced inter-core group delays in multicore fibers

Viktor Tsvirkun, Siddharth Sivankutty, Géraud Bouwmans, Olivier Vanvincq, Esben Ravn Andresen, Herve Rigneault

HAL Id: hal-01661281

https://hal.science/hal-01661281

Submitted on 12 Apr 2018

Bending-induced inter-core group delays in multicore fibers

VIKTOR TSVIRKUN,[1] SIDDHARTH SIVANKUTTY,[1] GÉRAUD BOUWMANS,[2] OLIVIER VANVINCQ,[2] ESBEN RAVN ANDRESEN,[2,3] AND HERVÉ RIGNEAULT[1,4]

[1]*Aix Marseille Univ, CNRS, Centrale Marseille, Institut Fresnel, F-13013 Marseille, France*
[2]*Univ. Lille, UMR 8523–Laboratoire de Physique des Lasers Atomes et Molécules, F-59000 Lille, France*
[3]*esben.andresen@ircica.univ-lille1.fr*
[4]*herve.rigneault@fresnel.fr*

Abstract: We examine the impact of fiber bends on ultrashort pulse propagation in a 169-core multicore fiber (MCF) by numerical simulations and experimental measurements. We show that an L-shaped bend (where only one end of the MCF is fixed) induces significant changes in group delays that are a function of core position but linear along the bending axis with a slope directly proportional to the bending angle. For U- and S-shaped bends (where both ends of the MCF are fixed) the induced refractive index and group delay changes are much smaller than the residual, intrinsic inter-core group delay differences of the unbent MCF. We further show that when used for point-scanning lensless endoscopy with ultrashort pulse excitation, bend-induced group delays in the MCF degrade the point-spread function due to spatiotemporal coupling. Our results show that bend-induced effects in MCFs can be parametrized with only two parameters: the angle of the bend axis and the amplitude of the bend. This remains valid for bend amplitudes up to at least 200 degrees.

References and links

1. A. J. Thompson, C. Paterson, M. A. A. Neil, C. Dunsby, and P. M. W. French, "Adaptive phase compensation for ultracompact laser scanning endomicroscopy," Opt. Lett. **36**, 1707 (2011).
2. E. R. Andresen, S. Sivankutty, V. Tsvirkun, G. Bouwmans, and H. Rigneault, "Ultrathin endoscopes based on multicore fibers and adaptive optics: a status review and perspectives," J. Biomed. Opt. **21**, 121506–121506 (2016).
3. T. Čižmár and K. Dholakia, "Exploiting multimode waveguides for pure fibre-based imaging," Nature Commun. **3**, 1027 (2012).
4. I. N. Papadopoulos, S. Farahi, C. Moser, and D. Psaltis, "Focusing and scanning light through a multimode optical fiber using digital phase conjugation," Opt. Express **20**, 10583 (2012).
5. Y. Choi, C. Yoon, M. Kim, T. D. Yang, C. Fang-Yen, R. R. Dasari, K. J. Lee, and W. Choi, "Scanner-Free and Wide-Field Endoscopic Imaging by Using a Single Multimode Optical Fiber," Phys. Rev. Lett, **109**, 203901 (2012).
6. S. Sivankutty, E. R. Andresen, R. Cossart, G. Bouwmans, S. Monneret, and H. Rigneault, "Ultra-thin rigid endoscope: two-photon imaging through a graded-index multi-mode fiber," Opt. Express **24**, 825 (2016).
7. D. Loterie, D. Psaltis, and C. Moser, "Bend translation in multimode fiber imaging," Opt. Express **25**, 6263 (2017).
8. A. M. Caravaca-Aguirre, E. Niv, D. B. Conkey, and R. Piestun, "Real-time resilient focusing through a bending multimode fiber," Opt. Express **21**, 12881 (2013).
9. S. Farahi, D. Ziegler, I. N. Papadopoulos, D. Psaltis, and C. Moser, "Dynamic bending compensation while focusing through a multimode fiber," Opt. Express **21**, 22504 (2013).
10. M. Plöschner, T. Tyc, and T. Čižmár, "Seeing through chaos in multimode fibres," Nature Photon. (2015).
11. I. Freund, M. Rosenbluh, and S. Feng, "Memory effects in propagation of optical waves through disordered media," Phys. Rev. Lett. (1988).
12. E. R. Andresen, G. Bouwmans, S. Monneret, and H. Rigneault, "Toward endoscopes with no distal optics: video-rate scanning microscopy through a fiber bundle." Opt. Lett. **38**, 609–11 (2013).
13. N. Stasio, D. B. Conkey, C. Moser, and D. Psaltis, "Light control in a multicore fiber using the memory effect," Opt. Express **23**, 30532 (2015).
14. E. R. Andresen, G. Bouwmans, S. Monneret, and H. Rigneault, "Two-photon lensless endoscope." Opt. Express **21**, 20713–21 (2013).

15. A. Porat, E. R. Andresen, H. Rigneault, D. Oron, S. Gigan, and O. Katz, "Widefield lensless imaging through a fiber bundle via speckle correlations," Opt. Express **24**, 16835 (2016).
16. V. Tsvirkun, S. Sivankutty, G. Bouwmans, O. Katz, E. R. Andresen, and H. Rigneault, "Widefield lensless endoscopy with a multicore fiber," Opt. Lett. **41**, 4771 (2016).
17. N. Stasio, C. Moser, and D. Psaltis, "Calibration-free imaging through a multicore fiber using speckle scanning microscopy," Opt. Lett. **41**, 3078–3081 (2016).
18. S. C. Warren, Y. Kim, J. M. Stone, C. Mitchell, J. C. Knight, M. A. A. Neil, C. Paterson, P. M. W. French, and C. Dunsby, "Adaptive multiphoton endomicroscopy through a dynamically deformed multicore optical fiber using proximal detection," Opt. Express **24**, 21474 (2016).
19. J. C. Roper, S. Yerolatsitis, T. A. Birks, B. J. Mangan, C. Dunsby, P. M. W. French, and J. C. Knight, "Minimizing Group Index Variations in a Multicore Endoscope Fiber," IEEE Photon. Tech. Lett. **27**, 2359 – 2362 (2015).
20. E. R. Andresen, S. Sivankutty, G. Bouwmans, L. Gallais, S. Monneret, and H. Rigneault, "Measurement and compensation of residual group delay in a multi-core fiber for lensless endoscopy," Journal of the Optical Society of America B **32**, 1221 (2015).
21. Y. Kim, S. C. Warren, J. M. Stone, J. C. Knight, M. A. A. Neil, C. Paterson, C. W. Dunsby, and P. M. W. French, "Adaptive Multiphoton Endomicroscope Incorporating a Polarization-Maintaining Multicore Optical Fibre," IEEE J. Sel. Top. Quantum Electron. **22**, 1–8 (2016).
22. S. Sivankutty, V. Tsvirkun, G. Bouwmans, D. Kogan, D. Oron, E. R. Andresen, and H. Rigneault, "Extended field-of-view in a lensless endoscope using an aperiodic multicore fiber," Opt. Lett. **41**, 3531 (2016).
23. S. Sivankutty, E. R. Andresen, G. Bouwmans, T. G. Brown, M. A. Alonso, and H. Rigneault, "Single-shot polarimetry imaging of multicore fiber," Opt. Lett. **41**, 2105 (2016).
24. R. T. Schermer and J. H. Cole, "Improved Bend Loss Formula Verified for Optical Fiber by Simulation and Experiment," IEEE J. Quantum Electron. **43**, 899–909 (2007).
25. W. Ye, D.-X. Xu, S. Janz, P. Cheben, M.-J. Picard, B. Lamontagne, and N. Tarr, "Birefringence control using stress engineering in silicon-on-insulator (SOI) waveguides," J. Lightw. Tech. **23**, 1308–1318 (2005).
26. V. Pratt, in "Proceedings of the 14th Annual Conference on Computer Graphics and Interactive Techniques - SIGGRAPH '87," (ACM Press, 1987).
27. R. Ulrich, S. C. Rashleigh, and W. Eickhoff, "Bending-induced birefringence in single-mode fibers," Opt. Lett. **5**, 273 (1980).
28. T. Tanab, F. Kannari, F. Korte, J. Koch, and B. Chichkov, "Influence of spatiotemporal coupling induced by an ultrashort laser pulse shaper on a focused beam profile," Appl. Opt. **44**, 1092–1098 (2005).
29. M. Coughlan, M. Plewicki, and R. J. Levis, "Spatio-temporal and -spectral coupling of shaped laser pulses in a focusing geometry," Opt. Express **18**, 23973–23986 (2010).

1. Introduction

In recent years challenges were tackled on the way towards robust fiber-based minimally invasive lensless endoscopes that would ultimately operate in a clinical setting. Both multicore [1, 2] (MCF) and multimode fibers [3] (MMF) have been considered together with wavefront shaping devices providing the ability to control the relative phase between the different injected fiber modes. MMF are appealing for their commercial availability, their small diameter (∼100 μm) and their large number of modes that can be used for focusing [4] and imaging [5, 6]. When dealing with flexible endoscopes phase control through MMF has been challenging because the fiber transmission matrix (TM) is strongly altered when the fiber is bent. Interestingly, recent works have identified parameters and regimes where deformation-induced changes in the TM can be minimized [7], measured and compensated for dynamically (in limited conditions) [8, 9] or even predicted [10], which brings hope to build MMF-based flexible lensless endoscopes. MCF, in strong contrast with MMF, are made with a multitude of single mode fiber cores which show weak or zero coupling, they maintain and translate, to some extent, their output diffraction patterns when a simple phase tip and/or tilt is applied on the input wavefront. This so-called "memory effect" [11] has been extensively used for imaging using scanning [12–14] or wide field modalities [15–17]. Because a freely moving distal end is expected to deform and compress the MCF inner and outer curvature sides, respectively, it was noted that a slight angular bend (< 3°) causes tip and tilt to be added to the phase profile at the distal tip of the MCF [13, 18], similar to the memory effect. Hereinafter we refer to this type of deformation as an L-type bend. When dealing with ultrashort pulses, the bending may also affect the group delays between pulses traveling in the different fiber cores such that they don't overlap and interfere anymore at the

distal tip [19, 20], precluding any focusing and imaging. This deformation-induced inter-core group delays are important in the context of 2-photon flexible lensless endoscope [14, 21] that might ultimately require active phase [18] and group delay controls [20].

In the scope of designing and building flexible lensless 2-photon endoscopes, this paper investigates numerically and experimentally the deformation-induced inter-core group delays resulting from bending MCFs with large (up to 200°) angular bends and assesses the impact on imaging performances. We concentrate our investigation on MCFs showing virtually no core-to-core coupling and having an infinite memory effect [22].

2. Methods

2.1. Experiments

Our experimental set-up (Fig. 1) utilizes phase-stepping spectral interferometry to measure delays between the ultrashort pulses, transmitted through the cores of interest, with respect to the reference core, as detailed in [20]. The output beam from a femtosecond laser source (Amplitude Systèmes t-Pulse, $\lambda = 1030$ nm, $\tau = 170$ fs, repetition rate 50 MHz) is expanded with a telescope (not shown) to overfill the aperture of a spatial light modulator (Hamamatsu LCOS-SLM X10468-07). The SLM is used to shape the wavefront entering each of the MCF cores at its proximal facet, relayed via a lens L1 and a microscope objective MO1 (Olympus Plan N, 20x NA 0.40). Transmitted light is collected from the MCF distal end using a 10x NA 0.25 microscope objective MO2 (Nikon Plan) and filtered with a linear polarizer LP (Thorlabs LPNIR100) to ensure maximum contrast of the interference fringes, as the output states of polarization in the MCF under study are random [23]. Distal facet is imaged with a lens L2 onto a camera CCD1 (FLIR FL3-U3-32S2M-CS) in order to monitor the evolution of the transmitted
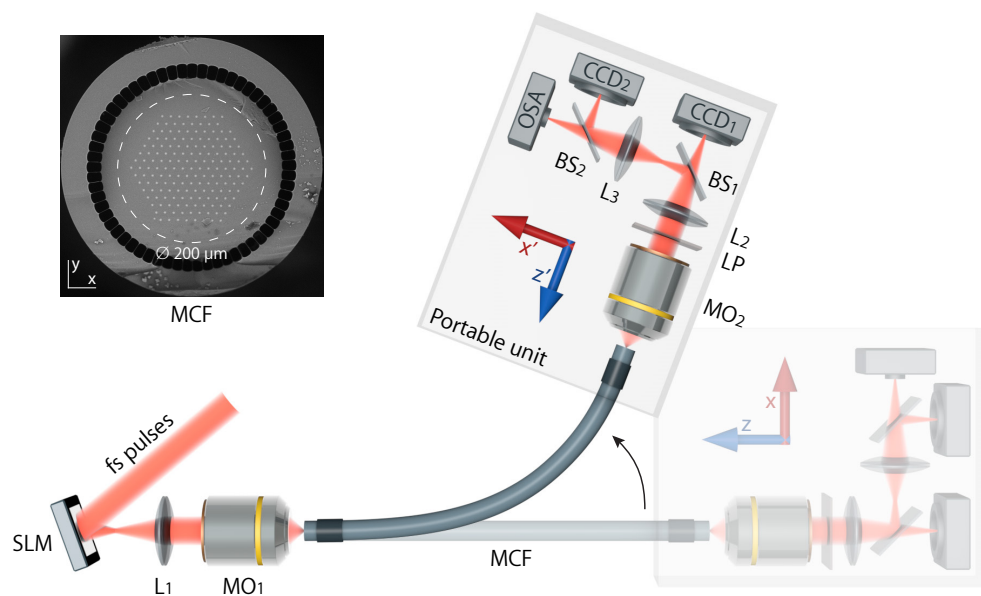

Fig. 1. Schematic of the setup used in bending experiments. SLM, spatial light modulator; L, lens; MO, microscope objective; MCF, multicore fiber; LP, linear polarizer; BS, beam splitter; CCD, charge coupled device; OSA, optical spectrum analyzer. The MCF (represented in blue gray) is clamped at both ends along approximately 1 cm long sections. Inset: SEM image of the MCF (cross-section) used in the experiments. Dashed white line delimits ⌀ 200 μm circumference.

power during fiber bending. Far field of the distal end face (via a lens L3) is coupled into a multimode fiber (core diameter 62.5 μm), which relays it to an optical spectrum analyzer OSA (Yokogawa AQ-6315A). Magnification in this configuration is chosen so that only a part of the far field much narrower than the spatial interference fringe is spatially selected with the MMF probe ($k_x D > 2\pi$, where k_x corresponds to the fringe spatial frequency and D is the inner probe diameter). We use phase-shifting spectral interferometry technique, previously described in Ref. [20], to measure the inter-core group delays in the MCF. The entire far-field interference pattern is imaged onto a camera CCD2 (Thorlabs DCU223M) to record the point spread function (PSF) of the fiber imaging system for different bending conditions. The entire distal detection part, including the clamped MCF distal end, is mounted onto a portable unit allowing its translation in xz plane (see Figs. 1, 6). Bent fiber geometry is recorded with a mobile camera (Appendix A provides an example of such recording).

Inset in Fig. 1 depicts the MCF study, which was described in [14]. Note that this MCF exhibits very low cross talk between its cores (< -25 dB). The MCF was fabricated with the following parameters: Ge-doped single-mode cores with a parabolic refractive index profile (maximum difference of 0.0031 compared to silica) and mode field diameter of 3.6 μm, triangular lattice pitch 11.8 μm and the outer diameter of 357 μm (including the double cladding). The total length of the MCF used in the experiments is approximately 300 mm.

2.2. Simulations

We perform the bent fiber simulation using the curvature loss formula, typically employed to predict the bending losses in both single mode and multimode fibers [24]. We consider two main effects which induce additional group delays across the MCF face – the fiber elongation/compression in the circular bend and the local refractive index change due to stress-optic effect upon bending. A circularly curved segment of the fiber is transformed to an equivalent straight one via conformal mapping. The modified refractive index distribution across the fiber cross-section is given by the following [24]:

$$n'(x, y) = n(x, y) \left[1 - n(x, y)^2 \frac{x}{2R} \left[p_{12} - \nu (p_{11} + p_{12}) \right] \right] \exp\left(\frac{x}{R}\right), \qquad (1)$$

where $n(x, y)$ is the refractive index of the unperturbed waveguide structure, R is the radius of curvature, ν is the Poisson's ratio, and p_{11}, p_{12} are the photoelastic tensor components. The exponential term accounts for the change in optical path length, whereas the term in the square brackets describes the changes to the physical refractive index with the photoelastic effect.

We consider a 300 mm long cylinder of 200 μm diameter made of silica with the following material properties: Poisson's ratio $\nu = 0.17$, refractive index of stress-free material $n = 1.45$ (fused silica for $\lambda = 1030$ nm) and photoelastic tensor elements $p_{11} = 0.16$, $p_{12} = 0.27$ (the latter are also wavelength-dependent, the closest values we found in literature are for $\lambda = 1150$ nm [25]). For the given values of material properties the geometric change is more significant than the stress-optical contribution. Three characteristic types of bends were studied as the ones most commonly encountered in the experimental conditions. In this article they are referred to as L-, U- and S-type geometries and are produced by applying a force $\vec{F}$ as shown schematically in Fig. 2.

For the sake of simplicity, only F_x component was chosen to be non-zero, and adjusted to produce displacements of the same magnitude [Figs. 2(a)–2(c)], reflecting the experimentally achievable ones. Fixed constraints are defined at the input fiber facet (L-type bend) and at both end facets for U- and S-bend cases. For the forces applied to xy cross-sections at the corresponding z positions as shown in Fig. 2, we trace the resulting deformed geometries and calculate the total bend-induced group delays $\Delta[\Delta\tau_i]$ using Eq. (1) and a least-squares curve fitting [26] to estimate the local radii of curvature along the fiber. $\Delta[\Delta\tau_i]$ is calculated as $(\text{OPD}_{i0} - \text{OPD}_i)/c$, where c is the speed of light, OPD_i is the optical path difference between the central and the ith core due

to local length and refractive index changes upon bending, and OPD_{i0} is the intrinsic OPD for the ith core (equals to zero in simulations).

Substituting the values of material properties into the stress-optic term of Eq. (1) and replacing the exponential by its first-order Taylor expansion, we can estimate the bend-induced delays by integrating along the fiber:

$$\Delta[\Delta\tau_i] \approx 0.79\frac{nx}{c}\int\frac{1}{R}\,\mathrm{d}s, \tag{2}$$

where s is a curvilinear abscissa ($\mathrm{d}s^2 = \mathrm{d}x^2 + \mathrm{d}y^2 + \mathrm{d}z^2$ in Cartesian coordinates). We can further substitute $\mathrm{d}s/\rho = \mathrm{d}\alpha$, where α is the turning angle. Hence we obtain

$$\Delta[\Delta\tau_i] \approx 0.79\frac{nx}{c}\Delta\alpha, \tag{3}$$

where $\Delta\alpha$ is the variation of angular increase along the curve formed by the fiber, i.e. $\Delta\alpha = \Delta\alpha_n - \pi$, where α_n denotes an angle between outward-pointing normal vectors of proximal and distal MCF facets for a deformed fiber geometry without loops. $\Delta\alpha$ is referred to as "bending angle" in this paper.
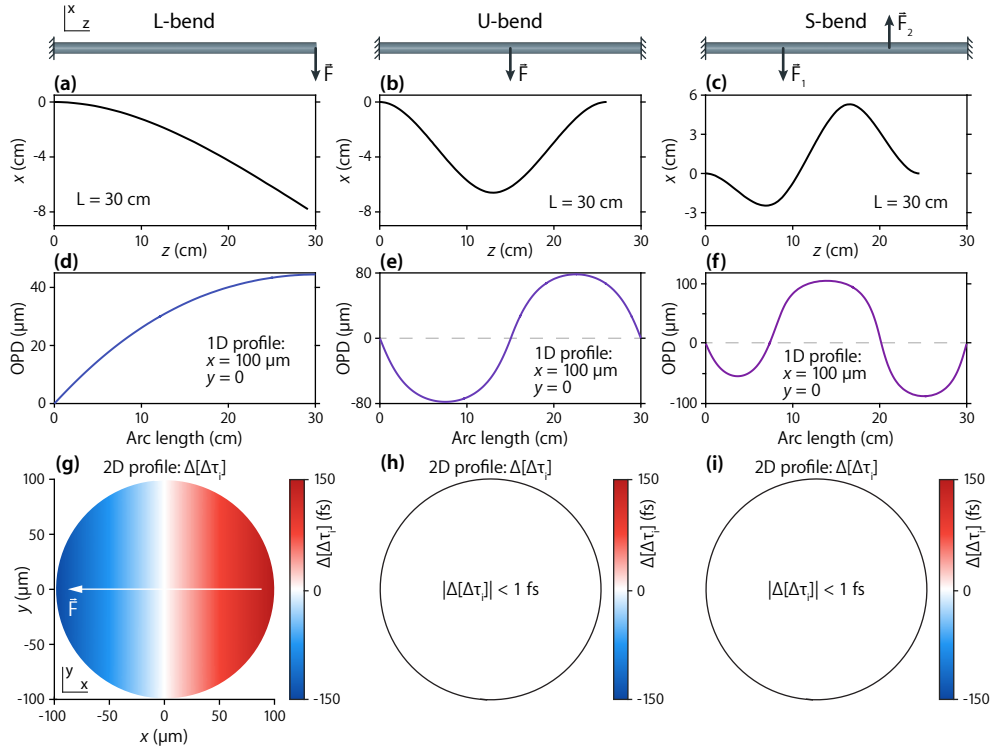

Fig. 2. Simulations of bending-induced group delays in different bending configurations. MCF (in blue gray) is depicted in its initial state with fixed constraints and the points where force $\vec{F}$ is applied. For each of the three configurations the resulting deformed geometry (a–c) and the induced group delays $\Delta[\Delta\tau_i]$ (g–i) are plotted. Examples of 1D evolution of the optical path difference (OPD) with respect to the central core are traced along the light propagation direction (d–f).

3. Results

3.1. Simulations

Inter-core group delays due to bending are expected to arise from the refractive index inhomogeneity among the cores and change in physical length. Therefore, in our simulations we estimated the group index change across the MCF face, and calculated the total accumulated optical path difference (OPD) and the corresponding $\Delta[\Delta\tau_i]$ (since the group index only exhibits linear longitudinal variations). The model fiber diameter was chosen to be comparable with the circumference which includes the cores in our sample MCF (see inset in Fig. 1).

The simplest bending geometry, which we refer to as L-bend, is simulated by applying a force to the distal fiber end while the proximal end is fixed [Fig. 2(a)]. OPD change along the arc length (z axis in the unperturbed geometry) for a given x, y [Fig. 2(a)] represent the situation for one MCF core, taken at the same coordinates. Finally, we calculated the spatial distribution of $\Delta[\Delta\tau_i]$, allowing to retrieve the induced group delay for any given location (x, y) of the core within the MCF [Fig. 2(g)] with respect to the central core.

The same type of simulations was next performed for the remaining two types of bending, whose denominations were inspired by the corresponding deformed geometry shapes [Figs. 2(b)–2(c)]. In the case of U-bend, the force is applied at $z = 15$ cm plane, producing a symmetric displacement and OPD distributions along the fiber length [Figs. 2(b), 2(e)]. When estimating the total $\Delta[\Delta\tau_i]$, it resulted in a cancellation of bending-related effects such that across the fiber face its maximum absolute change is less than 1 fs, most likely reflecting the numerical error of the curve fitting procedure. In the case of the S-bend, two forces of opposite directions and different magnitude were applied at 1/3 and 2/3 of the fiber length, which resulted in the asymmetric deformed geometry and OPD distributions along the fiber [Figs. 2(c), 2(f)]. Nevertheless, the overall $\Delta[\Delta\tau_i]$ along the total MCF length is very small (< 1 fs) and can be interpreted as the numerical error – as in the case of U-type deformation, see Fig. 2(i)].

All the above calculations were performed using Eqs. (1) and (2). Note that we obtain the same results as the ones displayed in Figs. 2(g)–2(f), using Eq. (3) and substituting $\Delta\alpha = 22°$ for L-bend and $\Delta\alpha = 0$ for U- and S-type geometries, and this without the need to integrate over the changing radii of curvature along the deformed fiber.

3.2. Experiments

Measurements of induced inter-core group delays for each type of bending geometry are shown in Figure 3. To have a precise estimation of the bending-related inter-core group delays, we first perform a calibration of the intrinsic GDD (relative to the fabrication process and material imperfections), the MCF being kept straight in its reference geometry, then this intrinsic GDD $\Delta\tau_i$ is subtracted from the subsequent inter-core group delays measurements while bending the MCF to give $\Delta[\Delta\tau_i]$. Figure 3(b) displays an example of MCF inter-core group delays $\Delta\tau_i$ spatial distribution, measured for an MCF held relatively straight in its reference geometry [Fig. 3(a)]. Measurements from the cores with low SNR were discarded; the displayed data covers 125 out of 169 cores. For the intrinsic GDD measurement we obtain a normal distribution $\Delta\tau_i$ with $2\sigma = 188$ fs [Fig. 3(c)], which is comparable to [20]. Subsequent measurement of the bending-induced inter-core group delays for the L-bend where the distal end was displaced by Δx of about 7.5 cm, is shown in [Figs. 3(d)–3(f)]. Measured bending-induced inter-core group delays spread (reference subtracted) follows a normal distribution with $2\sigma = 132$ fs [Fig. 3(f)] and $\Delta[\Delta\tau_i]$ values in Fig. 3(e) show a clear trend spanning from negative added delays to positive ones in the range of about ±150 fs over the entire MCF facet. Force in this experiment was applied along the negative direction of x axis (as indicated by the white arrow), and a qualitative agreement with the stress-induced refractive index simulation can be seen when comparing Fig. 3(e) and Fig. 2(d).
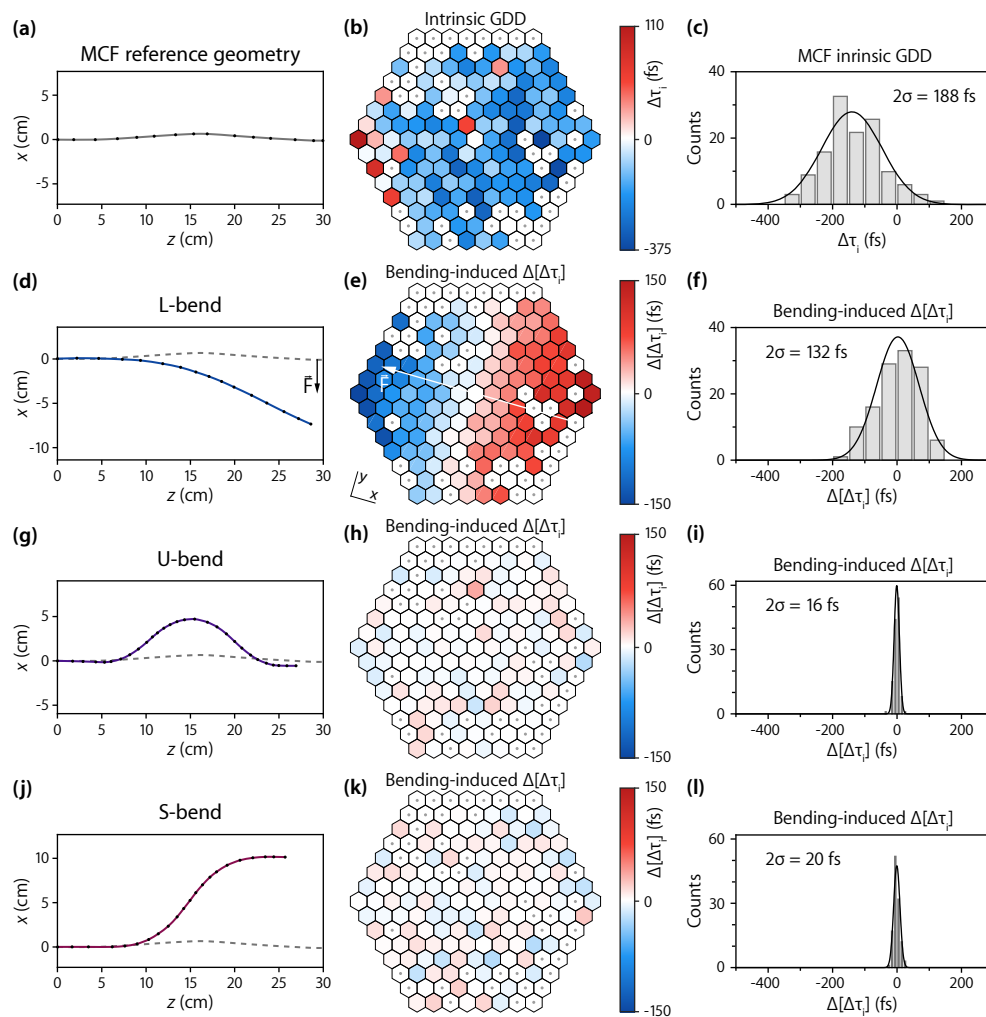
Fig. 3. Measurements of bending-induced inter-core group delays for different MCF bending configurations. For the measurement of the intrinsic group delay dispersion (GDD) (a–c) the MCF is held relatively straight; proximal ($z = 0$) and distal ($z = 30$ cm) end faces are parallel to each other. Intrinsic GDD (b) is color-coded so that each hexagon represents the relative delay $\Delta\tau_i$ between the central and an ith core according to the given color scale. Hexagons with centered gray dots represent the cores for which we could not perform reliable delay estimation (poor spectral fringe quality). Deformed MCF geometries in (d) L-, (g) U- and (j) S-bent configurations, plotted versus reference straight fiber (dashed gray). Black dots in (a,d,g,j) represent geometry points, extracted from the camera images of the MCF, taken from above the set-up. Bend-induced $\Delta[\Delta\tau_i]$ (e,h,k) calculated as a difference between $\Delta\tau_i$ values from bent and reference geometries. (f,i,l) show the corresponding $\Delta[\Delta\tau_i]$ spreads. Total delays spread (c) for the intrinsic GDD measurement is comparable to the probe laser pulse width (170 fs).
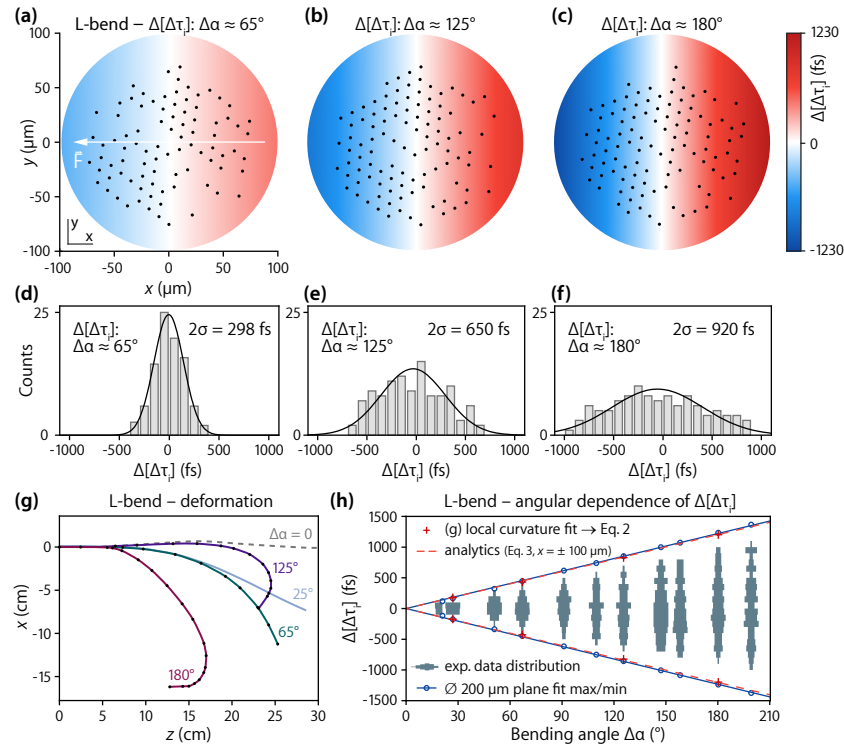
Fig. 4. Measurements of bend-induced inter-core group delays for L-type bending geometries. Surface plots (a–c) show plane fits of the experimental data (black dots), obtained for the relative angle change of distal end face of $\Delta\alpha \approx 65°$ (d), $125°$ (e) and $180°$ (f). (d–f) represent corresponding $\Delta[\Delta\tau_i]$ spreads of the experimental data. (g) Deformed geometries, used in this series of experiments, plotted alongside with the reference (dashed gray) and Fig. 3(d) (light blue) measurements. (h) Extrema values of $\varnothing\ 200\ \mu$m plane fits (circles – data, blue lines – linear fits) for $\Delta[\Delta\tau_i]$ measurements versus the bending angle $\Delta\alpha$ in L-type configuration. Violin plots (blue gray) represent normalized histograms for individual $\Delta[\Delta\tau_i](\Delta\alpha)$ datasets with the same binning as in (d)–(f). Red dashed line represents the analytical solution using Eq. 3 for the actual length of the MCF and two cores situated at $x = \pm100\ \mu$m as a function of $\Delta\alpha$. Red crosses represent $\Delta[\Delta\tau_i]$, calculated for the experimental deformed geometries in (g) using Eq. (2) for the varying R.

Measurements for U- and S-types of bending geometries are displayed in Figs. 3(g)–3(i) and Figs. 3(j)–3(l) correspondingly. We aimed to achieve displacements along the x axis similar to the L-bend case for an easier comparison between the obtained values. For both of the double-clamped geometries, we found that $\Delta[\Delta\tau_i]$ spreads show a marginal contribution with $2\sigma \leqslant 20$ fs, which we relate to the measurement uncertainty. Note that the error bars (three standard deviations) in presented GDD measurements using phase-stepping interferometry were below 20 fs for most of the cores. We scaled $\Delta[\Delta\tau_i]$ colorbars according to Fig. 3(e) (L-bend) experiment for easier comparison of the obtained values given that Δx fiber displacements are also comparable in all three cases. Here again the close to zero $\Delta[\Delta\tau_i]$ trend is in good agreement with the simulated results Figs. 2(h), 2(l).

We focused next on L-type bending, where the proximal and distal MCF facets are not parallel anymore. This is the situation similar to the real endoscopic operation where the distal MCF facet is free to move. As a geometrical parameter of the bend which reflects the evolution of $\Delta[\Delta\tau_i]$ spread magnitude we used $\Delta\alpha$, introduced earlier in Eq. (3). Therefore, our reference geometry measurement as well as U- and S-bends in Fig. 3 correspond to $\Delta\alpha = 0$ case and Fig. 3(e) (L-bend) to $\Delta\alpha = 25°$. We used spectral interferometry to perform $\Delta[\Delta\tau_i]$ evaluations for several $\Delta\alpha$ in the 0–200° range. Figures 4(a)–4(f) demonstrate three examples of such measurements for different $\Delta\alpha$ bending angles. Given the sparsity of the MCF core design and therefore of the associated recorded experimental data we used a plane fitting to achieve a more consistent comparison between datasets for different $\Delta\alpha$. In Figs. 4(a)–4(c) we display fitted $\varnothing$ 200 μm planes with the positions of experimentally obtained points given as black dots, scaled within ±1230 fs range of $\Delta[\Delta\tau_i]$. All three measurements of $\Delta[\Delta\tau_i]$ [see the bending geometries in Fig. 4(g)] exhibit a gradient along the bending axis, whose magnitude is proportional to the bending angle $\Delta\alpha$. As opposed to the first set of measurements (Fig. 3), now the added inter-core group delays exhibit larger $\Delta[\Delta\tau_i]$ distribution spreads, as can be observed in Figs. 4(d)–4(f). Figure 4(h) shows the data and fitting results for the whole set of measurements. Extrema values of plane fits on the $\varnothing$ 200 μm circle (blue circles) and their linear fits (solid blue lines) indicate a linear dependence of the induced $\Delta[\Delta\tau_i]$ span on the bending angle $\Delta\alpha$. Actual data distributions are represented by violin plots normalized by the maximum counts for each measurement and preserving the same binning ($-1500:100:1500$ fs) as in the histograms above [Figs. 4(d)–4(f)]. Dashed red lines trace the analytical dependency of $\Delta[\Delta\tau_i]$ versus the bending angle $\Delta\alpha$ for two virtual cores located at $x = \pm100$ μm. The red crosses show the examples of $\Delta[\Delta\tau_i]$ estimation for the above-mentioned virtual cores while extracting the local radii of curvature R for Eq. (2) from the experimental bent MCF geometries from Fig. 4(g). An example of such R fitting for $\Delta\alpha = 180°$ bending geometry is given in Appendix B. As it can be seen from the plots, bending-induced inter-core group delays can span as far as almost ±1 ps for $\Delta\alpha = 180°$ bend, which in turn would require a group delay compensating scheme such as a group delay controller (GDC) [20] to assure the temporal overlap of pulses at the distal MCF facet. For large bending angles one would expect to see some polarization mode dispersion [27]; therefore we performed all our measurements for a single polarization. Additionally, the bend radii in our experiments were kept sufficiently big in order to not induce a considerable bend loss (the transmitted intensity was continuously monitored with the CCD1 looking at the MCF distal facet).

The imaging performance of a 2-photon MCF lensless endoscope is directly related to the peak irradiance, requiring a spatially and temporally compact focal spot [14]. To assess the spatial aspect, we perform an investigation using CCD2 camera placed in the far field of the distal MCF facet (Fig. 1), and use the SLM to produce a distal focused spot [Fig. 5(a)]. In pulsed laser mode, bending-induced inter-core group delays reduce the number of temporally overlapping beamlets thus reducing the delivered power at the focus. As a figure of merit, we used an L-bent fiber with $\Delta\alpha = 180°$ together with the laser in CW operation regime so that individual beamlets from all the cores interfere and generate the brightest focal spot, with power P_{CW} [Fig. 5(d)]; against
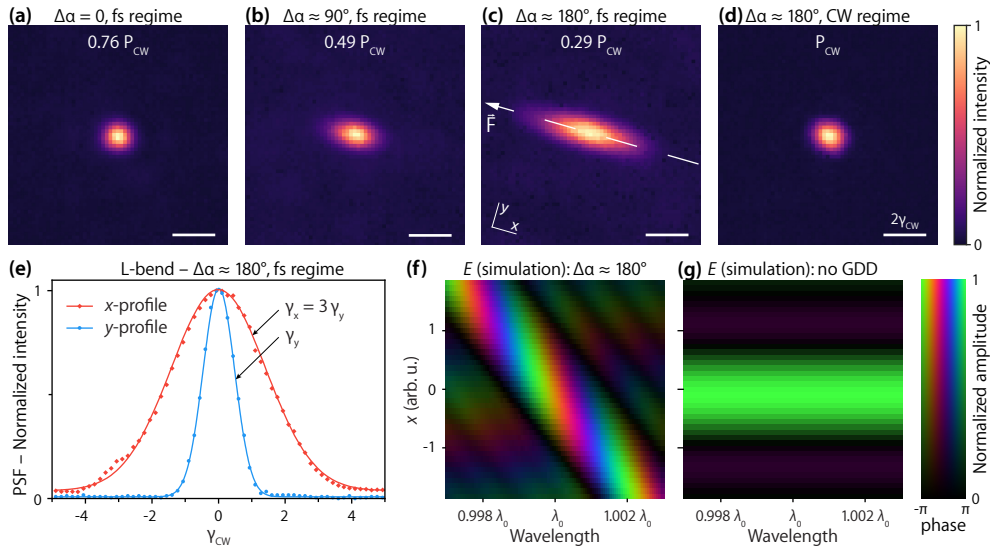
Fig. 5. (a–e) Measurements of bending-induced PSF changes in MCF for L-type geometries (normalized intensities). Multipliers of measured maximal intensity are given with respect to bending-insensitive (d) case, P_{CW}. (a–c) PSF in pulsed ($\tau = 170$ fs) and (d) continuous wave (CW) regimes of probe laser operation for $\Delta\alpha = 0$, 90 and 180° bends correspondingly. Dashed white line indicates the direction of applied force in the MCF reference frame. Scale bar, 2FWHM of PSF in CW regime. (e) Line profiles along x (red dots) and y (blue dots) axis for (c). FWHM values of the corresponding Gauss fits (solid lines) are indicated as $\gamma_{x,y}$. Far field E simulation using (f) experimental $\Delta[\Delta\tau_i]$ values for (c) case and (g) with $\Delta[\Delta\tau_i] = 0$. Colormap hue and brightness represent phase and normalized amplitude of the complex field correspondingly.

which the coherent combining of the ultrashort pulse will be evaluated for various bending angles. We now move to pulse laser mode ($\tau = 170$ fs) and investigate for various $\Delta\alpha$ the focus power loss resulting from bending-induced inter-core group delays. Figures 5(a)–5(c) show a significant drop from $0.76P_{CW}$ ($\Delta\alpha = 0$, intrinsic dispersion only) down to $0.29P_{CW}$ ($\Delta\alpha = 180°$). Increase of $\Delta\alpha$ therefore comes with a lower focal spot intensity, giving 49% ($\Delta\alpha = 90°$) and 29% ($\Delta\alpha = 180°$) of maximum possible power in the focus [Figs. 5(b), 5(c)] and therefore contributing to the increase of the background signal.

Emergence of a spatiotemporal effect due to added inter-core group delays can be easily observed from Figs. 5(a)–5(c), where the PSF evolves from a circular to an elliptical shape. This can be intuitively inferred from the anisotropy of the OPD change due to bending along only one axis. In other words, the large bending-induced inter-core group delays focus the various frequencies within the spectral width of the pulse into different spatial spots; this effect is reminiscent of the time-space coupling as observed in temporal pulse shapers [28, 29]. With this one observes a bending-induced distortion of the focal spot in Figs. 5(c), 5(e) where its full width at half maximum (FWHM) γ along the bending axis γ_x is 3 times larger than along y axis for $\Delta\alpha = 180°$ L-bend (Appendix A).

We illustrate this effect by calculating the far field distribution from the known intensity and group delay data at MCF distal facet. Figure 5(f) shows the complex field E distribution for the given laser bandwidth, simulated along the bending (x) axis in the CCD2 plane, with the experimentally measured $\Delta[\Delta\tau_i]$ values taken into account. Note that different wavelengths get focused (come in phase) at different spatial coordinates. This is analogous to the broadening of an interference fringe due to partial coherence, in this case along the bending axis. Note that

on the experimental data, along the orthogonal axis, the fringe width is still diffraction limited. Figure 5(g) represents a simulated case with no added inter-core group delays, resulting in a fully coherent state, thus retaining a symmetric and diffraction limited focus.

4. Discussion

The first important conclusion that can be drawn from the data presented in Figs. 2, 3 is that only the L-type bending geometry has a considerable impact on the inter-core group delays in the studied MCF. Both U- and S-bends exhibit a self-compensation of the bend-induced inter-core group delays on a scale of the entire fiber length, not affecting the total group delays spread. Second, in the case of L-bends, the added spatial inter-core group delays follow a linear law $\Delta[\Delta\tau_i] = ax_i$, where the slope a depends on the bending angle $\Delta\alpha$, and x_i is ith core coordinate along the bending axis. More generally, for a given $\Delta\alpha$ and known MCF length one can have an estimate of $\Delta[\Delta\tau_i]$ for an arbitrary location (x, y) whose precision depends mainly on the bending angle estimation error. $\Delta[\Delta\tau_i]$ dependence was found to be linear versus bending angle $\Delta\alpha$, as shown in Fig. 4(h) and from Eq. (1) for a constant L and substituting $R = L/\Delta\alpha$. One would expect the same behavior during fiber bending along y axis (generally speaking, along any direction in xy plane), assuming isotropic material properties. Additionally, experimental data in Figs. 4(g), 4(h) indicates that parameter a depends only on the angle between fiber end faces and not on the radius of curvature or relative position of input and output facets. For large angles of the L-bend and with femtosecond pulses, we found that spatial $\Delta[\Delta\tau_i]$ distribution affects the imaging system PSF through the loss of coherence between some of the delivered pulses, precluding several cores from contributing to the generation of the interferometric focal spot and thus lowering the delivered peak power. Both these characteristics become crucial when such fibers are employed for nonlinear imaging (such as 2-photon for instance) and therefore a group delay controller [20] covering $\Delta[\Delta\tau_i]$ range for the maximum bending angle would be required to ensure constant imaging performance in a flexible lensless endoscope set-up.

5. Conclusion

We experimentally studied multiple MCF bending geometries in terms of ultrashort (fs) pulse delivery and imaging performance. U- and S-type bends, even for large displacements, did not induce any significant additional inter-core group delays, whereas the added inter-core delays in L-type bending geometry depend linearly on the angle between distal and proximal fiber facets and the core coordinate along the bending axis. When using ultra-short pulses, imaging performance in terms of focal spot quality degrades for large bending angles when one fiber end is moving freely, requiring an active inter-core group delay compensation in the picosecond range in order to secure a stable and diffraction-limited imaging performance. These trends show a good agreement with a simple linear model (Eq. (3)) for the inter-core group delays as predicted by our simulations, where the bending-induced refractive index change for a single-clamped bending geometry (L-type) varies linearly along the bending axis with zero dispersion line crossing the fiber face at its middle, perpendicular to the applied stress. Simulations of the bending geometries where both ends are fixed display axial symmetry of bending-induced refractive index change, resulting in no significant dispersion of mean refractive index along the total fiber length. Our investigations highlight the suitability of MCFs for highly miniaturized, robust and flexible multi-photon endoscopes that could ultimately operate in clinical settings.
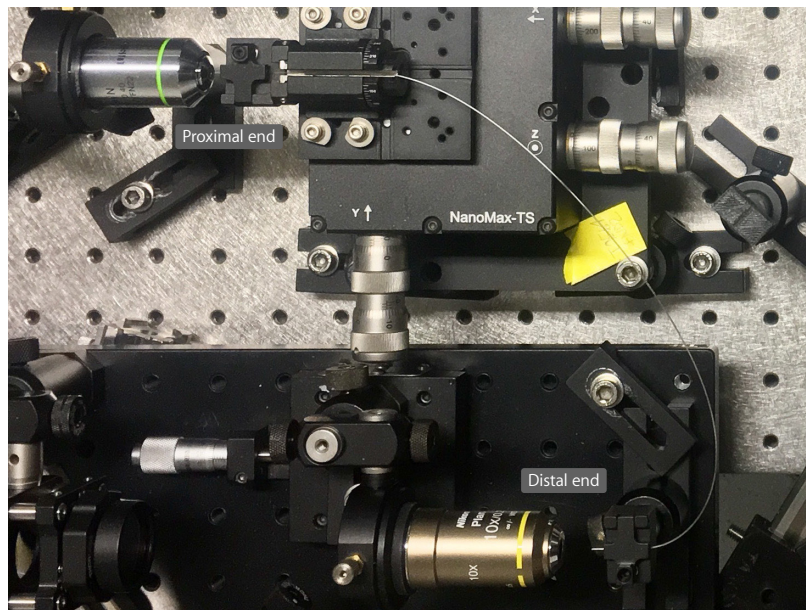
Appendix A: Top view of a bent MCF

Fig. 6. Top view of a part of the experimental set-up showing the 180°-bent MCF.

Appendix B: Example of the local curvature fitting for a known bending geometry
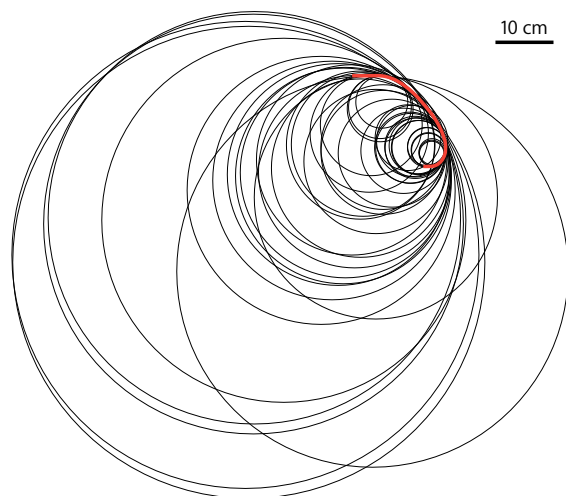

Fig. 7. Example of the circle fitting procedure for the estimation of bending-induced $\Delta[\Delta\tau_i]$ using Eq. 2. Deformed geometry from Fig. 4(g) with $\Delta\alpha = 180°$ (red line) and the fitted circles (black) for all the curve segments except the straight lines ($R \rightarrow \infty$).

Funding